

Application of Quantitative Fluorescence and Absorption-Edge Computed Microtomography to Image Metal Compartmentalization in *Alyssum murale*

DAVID H. MCNEAR, JR.,^{*,†}
EDWARD PELTIER,[†] JEFF EVERHART,[†]
RUFUS L. CHANEY,[‡] STEVE SUTTON,^{§,||}
MATT NEWVILLE,[§] MARK RIVERS,^{§,||} AND
DONALD L. SPARKS[†]

Environmental Soil Chemistry Research Group, Department of Plant and Soil Sciences, 152 Townsend Hall, University of Delaware, Newark, Delaware 19717-1303, USDA-ARS, Animal Manure and Biproducts Laboratory, Beltsville, Maryland 20705, University of Chicago, Consortium of Advanced Radiation Sciences, Advanced Photon Source, GSECARS, Argonne, Illinois 60439 USA, and Department of Geophysical Sciences, University of Chicago, Chicago, Illinois 60637

This paper shows that synchrotron-based fluorescence and absorption-edge computed microtomographies (CMT) are well-suited for determining the compartmentalization and concentration of metals in hyperaccumulating plant tissues. Fluorescence CMT of intact leaf, stem, and root samples revealed that Ni concentrated in stem and leaf dermal tissues and, together with Mn, in distinct regions associated with the Ca-rich trichomes on the leaf surface of the nickel hyperaccumulator *Alyssum murale* "Kotodesh". Metal enrichment was also observed within the vascular system of the finer roots, stem, and leaves but absent from the coarser root, which had a well-correlated metal coating. Absorption-edge CMT showed the three-dimensional distribution of the highest metal concentrations and verified that epidermal localization and Ni and Mn co-localization at the trichome base are phenomena that occurred throughout the entire leaf and may contribute significantly to metal detoxification and storage. Ni was also observed in the leaf tips, possibly resulting from release of excess Ni with guttation fluids. These results are consistent with a transport model where Ni is removed from the soil by the finer roots, carried to the leaves through the stem xylem, and distributed throughout the leaf by the veins to the dermal tissues, trichome bases, and in some cases the leaf tips.

Introduction

The search for an economically viable alternative to conventional remediation of heavy metal enriched soils has led

* Corresponding author phone: (302)831-1230; fax: (302)831-0605; dmcnear@udel.edu.

[†] University of Delaware.

[‡] USDA-ARS.

[§] Consortium of Advanced Radiation Sciences, University of Chicago.

^{||} Department of Geophysical Sciences, University of Chicago.

to the use of specialized metal accumulating plants (1–4). Metal hyperaccumulators have long been identified (5), but only recently have attempts been made to elucidate the physiological and biochemical mechanisms these plants use to accumulate and compartmentalize excess metals (6–9). A greater understanding of these processes could aid in increasing the efficiency of natural metal accumulators or in the engineering of specialized crops capable of impeding or accelerating metal uptake. Deciphering which plant tissues store metals is one step in understanding the sequestration mechanism(s). Current approaches for determining the compartmentalization of metals in plant tissues are limited by the use of techniques with low sensitivity, insufficient tissue specificity, or considerable sample handling and pretreatment requirements, the latter potentially altering the metal allocation (10–13). A tool that compliments the current methods, but can overcome some of their drawbacks, would be valuable in elucidating the mechanisms involved in metal hyperaccumulation by plants.

A majority of the previous studies on plant–metal compartmentalization use scanning electron microscopy with energy-dispersive X-ray analysis (SEM EDX) to decipher metal locations within plant tissues. SEM is very effective at resolving the cellular structures within plant tissues and when coupled with energy dispersive analysis can provide relative cellular elemental distributions including lighter elements (K, P, C, O) unattainable by other techniques. However, there are limitations involving sample preparation (e.g., freeze-drying, carbon-coating, etc.) and, because SEM is a surface-imaging tool, the need to section the tissues in order to get cross-sectional elemental distributions. These treatments have the potential to alter the chemical and physical elemental distribution of the metal within the plant tissues. In addition, the detection limits of SEM are quite high ($\sim 1000 \mu\text{g g}^{-1}$) which, while not as important for hyperaccumulating plants with typical dry matter metal concentrations well over $1000 \mu\text{g g}^{-1}$, may limit the identification of smaller but potentially relevant localizations.

Synchrotron X-ray fluorescence (SXRF) spectroscopy can overcome many of these limitations by providing in situ, highly sensitive, and well-resolved 2D elemental maps and, when coupled with X-ray absorption spectroscopy (XAS), the ability to determine the elemental species (13–15). However, because SXRF is 2D and the beam penetrates into or through the sample, the resulting SXRF image is actually a projection showing all of the entrained metals from one specific direction. Therefore, it may be difficult to tell exactly which compartment or specific tissue contains an observed metal-rich region. For instance, a face-on view of a leaf will show metals on both surfaces (top and bottom epidermal tissues) as well as those in the interior. Thus, a metal could be entrained in the top as well as the bottom dermal tissues, which would appear associated in the SXRF image but are instead separated by the thickness of the leaf. Therefore, because of these "thickness" effects, determining the compartmentalization of metals using SXRF should be done with caution and if possible, verified using another technique.

Synchrotron-based X-ray computed microtomography (CMT) can compensate for some of the drawbacks associated with using SXRF and SEM for imaging metal compartmentalization in plant tissues. Synchrotron-based X-ray absorption-edge and fluorescence CMT are techniques that utilize a high-intensity, tunable X-ray beam to nondestructively interrogate a sample as it is translated and/or rotated within the beam. The result, after computational reconstruction, is the cross-sectional two- and three-dimensional distributions

of specific elements within the sample. Unlike conventional X-ray CMT instruments, synchrotron-based fluorescence CMT can provide a highly resolved picture of the multi-elemental distribution through a virtual slice of the sample at concentrations down to approximately $1 \mu\text{g g}^{-1}$ (element dependent). Absorption-edge CMT provides a fully 3D image of the metal distribution, albeit, with some loss of resolution and sensitivity.

Application of these techniques has included imaging of various phenomena in earth and material sciences. For example, McLain et al. (16) used absorption-edge CMT to explore the association between cation sorption sites in alluvial soils, and Fe and pore-space distributions. They were able to do so by exposing the soils to a CsCl solution and then obtaining absorption-edge CMT images for Cs which revealed the location of the sorption sites. Absorption-edge CMT images of Fe then revealed the relation between sorption site, Fe, and pore-space distributions. In another application, Flynn et al. (17) used fluorescent CMT to investigate interplanetary dust collected from the Earth's stratosphere. They determined that the volatile elements Zn and Br were present not only on the surface but also in the core of the particle, indicating that the observed enrichments in these elements are indigenous rather than contaminants from the atmosphere. These studies highlight the utility of CMT techniques for deciphering elemental distributions in structurally sensitive samples.

The closest application of synchrotron tomographic techniques to biological systems relevant to this study were by Hansel et al. (18, 19) who used fluorescence CMT to help characterize Fe plaques and associated metals on the surface of roots from the aquatic plants *Phalaris arundinacea* (read canarygrass) and *Typha latifolia* (cattail). By use of this technique, they were able to determine that Pb and Fe accumulated on the surface of the root in a similar pattern, forming a covering on the root surface while As was isolated to distinct regions on the exterior and interior of the root. Similarly, Keon-Blute et al. (20) used fluorescence CMT to reveal that As was sequestered by Fe(III) oxyhydroxides within cattail root plaques from a contaminated wetland. However, these studies, because of the aquatic and metal excluding nature of the plants, were limited to the roots only. Additionally, no absorption-edge CMT technique was utilized to see if this characteristic was observed over the entire root length or just over the section chosen for analysis.

Therefore, the objective of this study was to show that synchrotron-based computed microtomographic techniques, including the novel application of synchrotron absorption-edge CMT, are effective at determining the metal compartmentalization and concentration throughout plant tissues and to do so by exploring the metal partitioning behavior of Ni within the shoots and roots of the Ni hyperaccumulator *Alyssum murale* "Kotodesh".

Experimental Section

Plant Sample Preparation. The soils and plants used in this study have been described and characterized elsewhere (21). Briefly, the known Ni hyperaccumulator *Alyssum murale* "Kotodesh" (common name yellowtuft) is an herbaceous perennial with upright growth habit from the Brassicaceae family and is native to serpentine soils throughout Mediterranean southern Europe. This ecotype has been proven to be an effective Ni hyperaccumulator through greenhouse and field trials and has been developed into a commercial crop for phytoremediation or phytomining (2, 22, 23). *Alyssum murale* used in this study was grown in a greenhouse using natural and artificial light, in Ni enriched loam soils (Welland soil, Typic Epiaquoll; Canadian classification, Terric Mesisol) collected from an area surrounding an historic Ni refinery in Port Colborne, Ontario, Canada. The soils containing

approximately 100 mg kg^{-1} and 2000 mg kg^{-1} Ni were sieved wet, mixed thoroughly, placed in 1.5-L plastic pots and allowed to equilibrate with fertilizers for one week. Seeds of *A. murale* were first germinated in Promix before being transplanted into the 1.5-L soil pots. Plants were harvested after approximately 120–180 days of growth. The roots used for analysis were removed from the pots and lightly washed with double deionized water to remove attached soil particles. Roots were examined under a light microscope to verify cleanliness.

Attempts were made to image "fresh" plant tissues using fluorescent CMT; however, it was found that shock freezing and partial drying was required because the high power density of the microfocused X-ray beam caused motion associated with dehydration in "live" *Alyssum* plant tissue which compromised reconstruction of the tomograms. As such, whole shoot sections were excised from the plants (grown in 100 mg kg^{-1} Ni soils) and immediately immersed in liquid nitrogen and dried under vacuum at $-180 \text{ }^\circ\text{C}$ for 24 h to prevent ice crystal formation. Shoots and roots were then taken to the beamline at which point the leaves were separated from the stem and attached to a wooden shaft using epoxy resin. The wooden shaft was then cut to $\sim 5 \text{ mm}$ in length and the cut end inserted into the rotation axis of an x - y - θ stepping sample stage for imaging. The roots were mounted in a similar way; however, the stems, because of their inherent rigidity, were simply inserted into a bead of modeling clay and attached to the stage. For absorption-edge CMT, living plants (grown in 2000 mg kg^{-1} Ni soils) were transported to the beamline and a leaf was removed just prior to analysis and mounted directly to the x - y - θ stage by placing the proximal (bottom) portion of the leaf into a bead of modeling clay.

SEM. SEM was used in an effort to obtain highly resolved cross-sectional images for correlating the metal compartmentalization observed in fluorescence CMT with specific plant tissues. Scanning electron micrographs were recorded using a Hitachi 4700 FESEM. Leaves from *A. murale* were freeze-dried as described above and then re-suspended in liquid nitrogen where they were fractured using forceps to acquire representative cross sections. Samples were then mounted on a conductive carbon stub and sputter coated with carbon prior to analysis. Samples were scanned manually at magnifications of 85 – $300\times$.

X-ray Fluorescence CMT. Thorough discussions on the fundamentals of tomographic instrumentation and techniques can be found elsewhere (24–27), and only a brief instrumental description is provided here. Samples were analyzed at the GeoSoilEnviroCARS (GSECARS) beamline at the Advanced Photon Source, Argonne National Laboratory (APS-ANL), Chicago, IL. For fluorescence CMT, the APS undulator (13-ID-C) source was used in conjunction with a cryogenically cooled, Si double-crystal monochromator, and Kirkpatrick-Baez microfocusing mirrors (28–30) to produce a $5\text{-}\mu\text{m}$ X-ray beam. X-ray fluorescence spectra were collected with a 16-element Ge array detector (Canberra Industries, Inc.) coupled with digital signal processing electronics (XIA, Inc.). Transmission tomograms were recorded simultaneously, resulting in a density profile of the leaf tissue, which provides an image of the plant tissue structure. Fluorescence microtomography data collection consisted of mounting the specimen on a rotation–translation stage, collecting XRF intensities as the specimen is translated through the X-ray beam, rotating by a small angle, repeating the translation–XRF collection, and continuing this process to encompass a total rotation of 180° . Typical datasets were collected with $5\text{-}\mu\text{m}$ translation steps over 1.5 mm , 3° angular steps, and dwell times of 1 s resulting in 2D "sinograms" (intensity on a "position-angle" plot) for each element with total collection times of $\sim 5 \text{ h}$. 2D element images were then computationally

reconstructed using fast Fourier transform based Gridrec software developed by Brookhaven National Laboratory (31), which was controlled by the IDL programming language (Research Systems, Inc.) yielding images of the cross-sectional internal metal distributions.

Absorption by the object of incoming X-rays and outgoing fluorescent X-rays can affect the reconstructed images thereby limiting the size of objects that can be imaged. The absorption is given by

$$\frac{I}{I_0} = e^{-\mu x} \quad (1)$$

where I_0 is the initial X-ray intensity and I is the intensity after passing a distance x (cm) through material of linear absorption coefficient μ (cm^{-1}). The coefficient μ depends on the composition of the material and the X-ray energy. In a fluorescence microtomography measurement, the incident energy is chosen to be well above the absorption-edge energies of the elements of interest, to excite the fluorescence from all elements of interest simultaneously. Consequently, absorption effects typically result from the absorption of the fluorescence X-rays (at lower energies than the incident energy) traversing the object on their way to the detector. By use of the equation above, the absorption of fluorescence X-rays of interest can be determined. A useful “rule of thumb” for the upper limit of “correctable” absorption is the factor e (≈ 2.7), a “characteristic absorption value”.

By use of the transmission tomograms collected simultaneously with the fluorescence tomograms for our partially dried samples and by assumption that the major sample composition was approximately cellulose (CH_2O , $\mu = 3.0 \text{ cm}^{-1}$ for 11 keV), the characteristic absorption length (length for an absorption factor of “ e ”) for the 11-keV incident X-rays is ~ 5 mm. The characteristic lengths for the fluorescence X-rays, Ca $K\alpha$ (3.7 keV), Mn $K\alpha$ (5.9 keV), Fe $K\alpha$ (6.4 keV), Ni $K\alpha$ (7.5 keV), and Zn $K\alpha$ (8.6 keV), were 0.2, 0.7, 0.9, 1.5, and 2.3 mm, respectively. Thus, the practical size limit for Ni $K\alpha$ fluorescence tomograms was about 1 mm. The maximum size of objects imaged was ~ 1 mm, i.e., near this limit.

Various algorithms have been or are being developed for correcting fluorescence microtomography data for absorption artifacts (32–34). In the present work, approximate absorption corrections were applied to fluorescence sinograms by using the transmission sinograms collected simultaneously to empirically determine the linear absorption coefficient μ of the absorbing material. Each sinogram is a plot of intensity (fluorescence or absorption) vs translation position and rotation angle. Each row (rotation angle) in the fluorescence sinogram was treated separately in the following way. First, the pixel representing the detector facing edge of the object was identified and defined as a reference point (X_0). At other pixels (translation position) in the row (X), the intensity $I_{f,0}$ was corrected to “no absorption” intensity $I_{f,x}$ by multiplying by an absorption factor ϕ_x . ϕ_x was calculated by first determining the average absorption $\bar{I}_{t,x}$ in the transmission sinogram (values of $I_t/I_{t,0}$) over the pixels between X and X_0 . The linear absorption coefficient at incident energy E_0 , μ_{x,E_0} (cm^{-1}) was then

$$\mu_{x,E_0} = -\ln(\bar{I}_t)/L_x \quad (2)$$

where L_x is the width of the object in the orthogonal direction (determined from the transmission sinogram). The linear absorption coefficient for a fluorescence X-ray E_f was determined from

$$\mu_{x,E_f} = \mu_{x,E_0} \left[\frac{\mu_{\text{cellulose},E_f}}{\mu_{\text{cellulose},E_0}} \right] \quad (3)$$

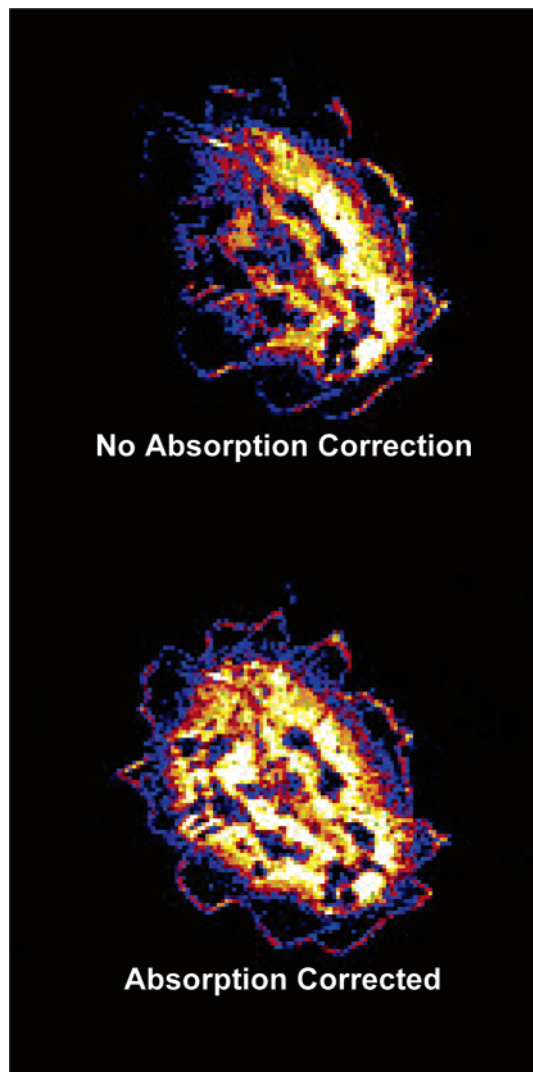


FIGURE 1. Nickel fluorescence microtomograms of the stem showing the result of absorption correcting the data. The top tomogram is uncorrected for absorption effects, while the bottom tomogram results from absorption correcting the fluorescent intensity. The X-ray fluorescence detector is located to the right in both cases.

where the cellulose coefficients were computed theoretically assuming a composition of CH_2O . Finally, the corrected intensity at pixel X is

$$I_{f,x} = \phi_x(I_{f,0}) = I_{f,0}e^{(\mu_{x,E_f}\Delta X)} \quad (4)$$

where $\Delta X = X - X_0$. In this way, absorption corrections were applied to each pixel in each fluorescence sinogram, and then reconstruction was performed on the corrected dataset. Figure 1 shows the result of applying this absorption correction algorithm to the Ni fluorescence tomogram of an *A. murale* stem.

The density ρ_x of the material-absorbing fluorescence X-rays from each pixel at translation position X was approximated by using the mass absorption coefficient for cellulose (CH_2O , $\mu/\rho = 3.0 \text{ cm}^2 \text{ g}^{-1}$ for 11 keV), in which case

$$\rho_x = \mu_{x,E_0} / (\mu/\rho)_{\text{cellulose},E_0} \quad (5)$$

The average of these density values was defined to be the object density ρ_{obj} .

Element concentrations were calculated for the fluorescence microtomograms by using measurements of the

SRM1832/33 (NIST) thin-film standards to obtain sensitivities (counts per second per $\mu\text{g cm}^{-2}$) for Ca, Mn, Fe, Cu, and Zn. The Fe and Cu sensitivities (different by a factor of 2) were then interpolated by atomic number to infer Ni sensitivity. This approach yielded mass per unit area ($\mu\text{g cm}^{-2}$) for a specific element at each pixel in the fluorescence microtomogram which, when divided by the beam size ($5\ \mu\text{m}$), gave the element density at each (i,j) pixel $\rho_{\text{el,obj}}(i,j)$. Element concentrations (weight fraction) $C_{\text{el,obj}}(i,j)$ were calculated using the object density ρ_{obj} (0.4, 1.3, and $0.6\ \text{g cm}^{-3}$ for the leaf, stem, and root, respectively), where

$$C_{\text{el,obj}}(i,j) = \rho_{\text{el,obj}}(i,j) / \rho_{\text{obj}} \quad (6)$$

For the leaf Ca microtomogram, a value of $2.5\ \text{g cm}^{-3}$ was used for object density (ρ_{obj}), based on the expectation that Ca resides in trichomes composed of calcite and/or calcium oxalate (average density of the two utilized). The concentrations determined in this way may be interpreted as dry tissue concentrations ($\mu\text{g g}^{-1}$). The concentration precision is typically ± 15 and $\pm 10\%$ (1σ), for individual and mean values, respectively.

Absorption-Edge CMT. The GSECARS bending magnet source (13-BM-D) provided a wide-fan X-ray beam for flood field applications used in absorption-edge CMT (26, 35). The monochromator was a narrow gap, Si(111) double-crystal instrument. The transmitted X-rays were converted to visible light with a single-crystal YAG scintillator, and the scintillator was imaged with a microscope objective ($10\times$) projected onto a 1300×1030 pixel fast charge-coupled device X-ray area detector (MicroMax) resulting in a field of view $2.15 \times 1.7\ \text{mm}^2$ and an optical resolution of $3.3\ \mu\text{m}$. Typical 3D datasets were collected with 0.5° steps over 180° and dwell times of 10 s. One tomogram was collected with the X-ray beam energy at 8300 eV, i.e., ~ 30 eV below the Ni K absorption edge (8333 eV), and a second tomogram was acquired above the Ni K edge. To enhance absorption contrast, the above-edge energy was selected to coincide with the X-ray absorption near-edge spectroscopy (XANES) white line for the Ni in the plant tissue (8350 eV). This energy was determined empirically by viewing the absorption radiograph in real time as the monochromator energy was scanned manually until the energy of maximum absorption was found. These two sinograms (above edge and below edge) were then subtracted, the difference matrix reconstructed using the Gridrec-based software (31), and the resulting images then stacked and viewed sequentially resulting in a movie depicting the metal distribution from the top (distal) to the bottom (proximal) end of the leaf. Typical image acquisition times with these settings were 45 min to 1.5 h.

The phase contrast in the transmission microtomography images is negligible. The region r in the sample that contributes to a point at the detector is given by (36)

$$r = \sqrt{\lambda D} \quad (7)$$

where λ is the X-ray wavelength, and D is the sample to detector distance.

In our setup, D is ~ 0.1 m and λ is $\sim 1\ \text{\AA}$ (10^{-10} m). Thus, r is $\sim 3\ \mu\text{m}$, i.e., comparable to our empirically determined resolution of $3.3\ \mu\text{m}$, suggesting that the phase contrast content of the transmission images is minimal. Furthermore, any phase contrast present in these images will cancel out during the image subtraction procedure since the difference in λ between the two images (corresponding to an energy difference of 50 eV out of 8300 eV) results in a change in r of $< 1\%$.

The Ni concentrations in the absorption-edge microtomograms were quantified by comparison with a theoretical absorption coefficient μ_0 (cellulose containing Ni at con-

TABLE 1. Leaf, Stem, and Root Metal Concentrations ($\mu\text{g g}^{-1}$) Calculated for the Fluorescent Tomograms in Figures 2 and 4

	dried tissue density (g cm^{-3})	element	max concn ($\mu\text{g g}^{-1}$)	mean concn ($\mu\text{g g}^{-1}$)	MDL ($\mu\text{g g}^{-1}$) ^a
leaf	0.4	Ni	2 700	500	18
		Fe	642	150	18
		Zn	464	95	18
		Ca	571 000	88 000	1 900
		Mn	1 250	200	18
stem	1.3	Ni	1 320	440	37
		Fe	37	11	5
		Zn	337	51	37
roots	0.6	Ni	19 000 (2 500) ^b	670	33
		Fe	110 000 (9 000) ^b	3 300	333
		Zn	1 700 (670) ^b	230	33

^a Minimum detection limit is defined to be the two standard deviation variability of the image background in each case. ^b Values in parentheses represent the Ni concentrations in the finer root shown in the inset of the root tomogram in Figure 4.

centration C_0 ; $1.1\ \text{g/cm}^3$; 8.35 keV) with the measured absorption coefficients where the Ni concentration at pixel (i,j) is

$$C(i,j) = C_0 \left(\frac{\mu(i,j)}{\mu_0} \right) \quad (8)$$

μ_0 includes an absorption coefficient enhancement factor (2.1) resulting from collecting the above-edge tomogram with the incident energy on the Ni K absorption-edge white line. This factor was determined empirically from a XANES spectrum collected on a similar Ni-accumulated *Alyssum* leaf. The Ni concentrations determined in this way are wet-tissue values ($\mu\text{g g}^{-1}$ wet tissue). The concentration precision is typically ± 10 and $\pm 5\%$ (1σ), for individual and mean values, respectively.

The Ni detection limit was calculated by taking the standard deviation of values in a relatively uniform, Ni-free, part of the difference image and comparing that absorption value (2σ) with the absorption expected from water containing 3% Ni (to convert to concentration). This resulted in a calculated Ni detection limit of about 0.5% or $5000\ \mu\text{g g}^{-1}$ wet tissue weight. To compare the wet weight with the dry weight values calculated by fluorescence CMT, a correction must be made to make up for the presence of water within the sample. The density value for the dry leaf tissue was calculated to be $0.4\ \text{g cm}^{-3}$ compared to the $1.1\ \text{g cm}^{-3}$ value used for the wet leaf, roughly a difference of 3. Therefore, to equate the absorption-edge to the fluorescence CMT concentrations, the absorption-edge values were multiplied by a factor of 3.

Results and Discussion

Leaf Metal Compartmentalization. Tabulated in Table 1 are the leaf, stem, and root metal concentrations ($\mu\text{g g}^{-1}$) calculated from the fluorescent tomograms in Figure 2. The mean Ca, Ni, Mn, and Zn concentrations in our leaf sample are $\sim 90,000, 500, 200,$ and $100\ \mu\text{g g}^{-1}$ dry weights, respectively. In whole leaves of *A. murale* "Kotodesh" plants grown in similarly enriched soils, Broadhurst et al. (37) found Ca, Ni, Mn, and Zn concentrations of $\sim 40,000, 2000, 125,$ and $140\ \mu\text{g g}^{-1}$ dry weight, respectively. The concentrations of Mn and Zn in the two studies are very similar; however, there is a slight difference in the Ni and Ca concentrations. These small differences most likely resulted from variations in the way the plants were grown, soil metal content, the age of the leaf, and/or differences in the mass of tissue sampled. The latter of these is of particular importance, because the metal concentrations detected by fluorescence CMT will be sensi-

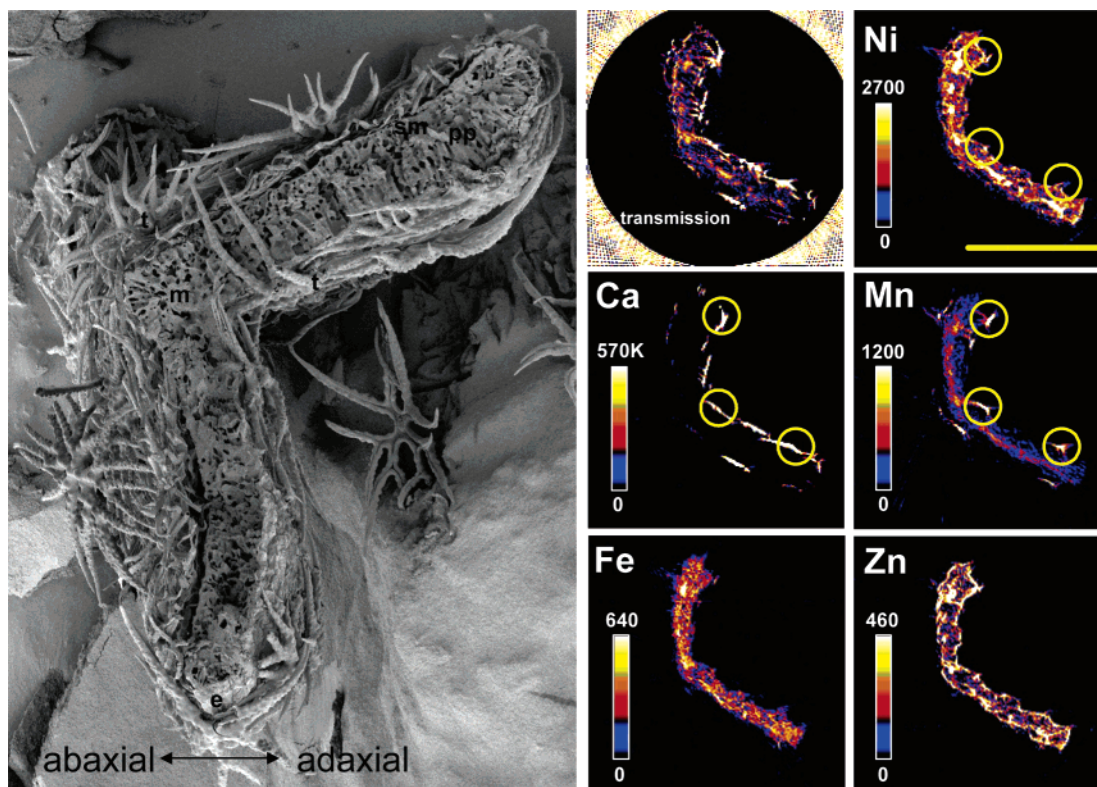


FIGURE 2. Fluorescent-computed microtomography images showing the Ni, Ca, Mn, Fe, and Zn distributions in an *Alyssum murale* “Kotodesh” leaf cross section. An SEM image showing a cross-section of an *A. murale* leaf is provided to highlight the internal architecture of the leaf and to aid in correlating the metal distribution in the fluorescent CMT images with specific leaf tissues (m, midrib; t, trichome; sm, spongy mesophyll; pp, palisade parenchyma; e, epidermis). The colorimetric scale maps region-specific relative metal concentrations ($\mu\text{g g}^{-1}$) for each element, with brighter colors indicating areas of higher enrichment. The lower thresholds for the tomograms were adjusted up slightly to suppress background noise and thereby improve image quality. In the transmission tomogram, brighter regions indicate tissues of higher density. Note that the Ca concentrations are in thousands. Yellow scale bar represents $\sim 500 \mu\text{m}$.

tive to the exact 5- μm slice chosen for analysis. For example, the Ca concentration will be highly influenced by how many Ca-rich trichomes the tomogram intersects. Nonetheless, the agreement between the two studies is a good indication that our calculated values provide a reasonable estimate of the average metal concentrations within *A. murale* tissues. Moreover, the tomograms have the added advantage of revealing the concentrations in specific tissues, crucial information in trying to understanding the mechanisms of metal compartmentalization and tolerance.

The highest Ni concentrations (Figures 1 and 2) are within the epidermal (upper and lower) and vascular tissues (up to $\sim 2700 \mu\text{g g}^{-1}$) with relatively little enrichment within the ground tissues (spongy mesophyll and palisade parenchyma, $< 680 \mu\text{g g}^{-1}$). Epidermal localization of metals in hyperaccumulating plants is commonly attributed to compartmentation of organic acid complexed metals within the vacuoles of epidermal cells (10, 38–40). The mechanism for the exclusion of excess Ni from the mesophyll and concentration in the epidermal vacuoles is still not clearly understood, however it may be both a physiological and/or defense-related response. In higher plants, a majority of the photosynthetic activity takes place within the mesophyll of the leaf (41), and as such, segregation of Ni from these tissues is essential to prohibit disruption of the metal-sensitive photosynthetic apparatus (42). Alternatively, Jhee et al. (43) suggested that hyperaccumulation may have evolved from selective pressure of insect herbivores and as such hypothesize that the plants are excluding Ni to the dermal tissues of the leaf to avoid insect damage. However, there is still little consensus as to the role of metals in preventing insect herbivory (44–47). Regardless, studies on several Ni hyper-

accumulators have identified histidine (7) and citrate (48–50) as the primary complexing ligands, and therefore, it is likely that they are playing the primary role in the detoxification and compartmentalization of Ni in *A. murale*.

The vascular tissues also exhibit high Ni concentrations, which can be seen in Figure 2 as discrete white/yellow areas within the interior of the leaf. Few studies have observed notable enrichment of the vascular bundles as was observed here. The presence of nickel within the vascular system (as well as Fe and Zn) is expected because the plant veins (xylem) are the primary mode of transport and delivery of metals to the leaves. We interpret the association of Ni with the vascular system as being due to entrainment during fixation, as opposed to tissue loading. Detection of entrained metals may have been facilitated by the analysis of intact vs sectioned and/or carbon-coated specimens. Admittedly, the resolution is only sufficient enough to elucidate enrichment of the vascular bundle and not the constituent tissues (tracheid or sieve cells, bundle sheath, etc.). However, there is little, if any, evidence as to the redistribution of Ni via phloem loading, and as such, it is more likely that Ni is being transported in the xylem, bound to organic ligands (histidine, citrate), and as hydrated Ni, from which it is then offloaded into the epidermal vacuoles for storage.

As can be seen in the SEM image (Figure 2), the abaxial and adaxial surfaces of the *A. murale* “Kotodesh” leaves are densely carpeted with stellate (starlike) trichomes. The trichomes are unicellular and comprised of a basal compartment, pedicle, and rays. Trichomes function to prevent water loss and potentially as a defense against insect herbivory (51). They are predominantly made of calcium oxalate or calcite (52) and as such show up quite clearly in the calcium

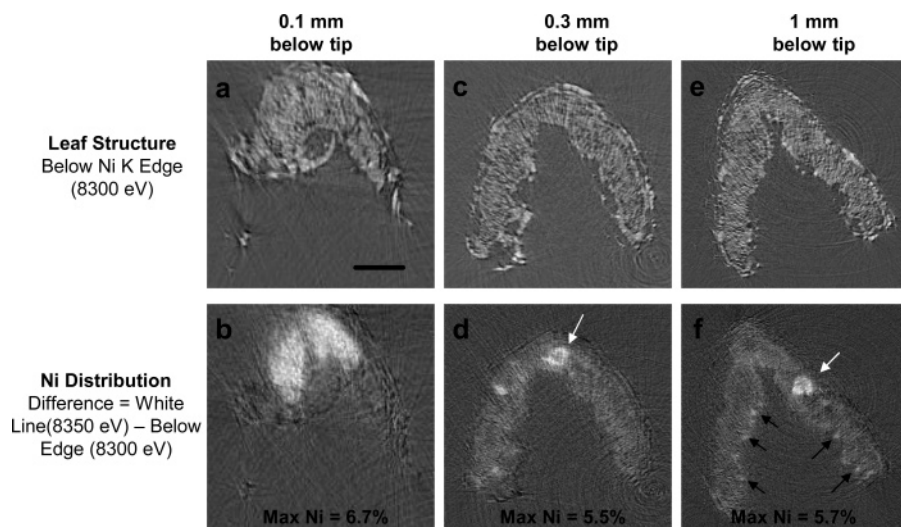


FIGURE 3. (a–f) Stop frames from the absorption-edge projection series showing the below-edge images depicting the leaf structure (a, c, and e) and the subtracted (above (8350 eV) – below (8300 eV)) images showing the Ni distribution (b, d, and f) from 0.1 (a and b), 0.3 (c and d), and 1 mm (e and f) below the *Alyssum murale* “Kotodesh” leaf tip. Maximum Ni concentrations in the 0.1, 0.3, and 1 mm sections are 6.7, 5.5, and 5.7 wt %, respectively. Black arrows indicate regions of Ni enrichment on the leaf surface while white arrows indicate Ni concentrations within the veins. The scale bar represents $\sim 250 \mu\text{m}$.

tomograms as bright spots on the surface of the leaf (Figure 2). The mean Ca concentration is $\sim 90,000 \mu\text{g g}^{-1}$ (or 9%) with concentrations exceeding $500,000 \mu\text{g g}^{-1}$ dry tissue (or 50%) in select pixels. Mn is absent or below detection throughout the bulk of the epidermal tissues, with the exception of highly concentrated spots that coincide with Ca (trichome) and possibly Ni on the leaf surface (circles in Figure 2). There is still no clear consensus as to whether trichomes on the surface of hyperaccumulating plants serve as a repository for metals (10, 11, 39, 53, 54). Our tomograms are consistent with the results of a recent study by Broadhurst et al. (37) who demonstrated that the trichome pedicle, trichome basal compartment, and the epidermal cells adjacent to the trichomes of *A. murale* “Kotodesh” were significantly enriched with both Ni and Mn, while the rays were only enriched in Ca. An X-ray bit map showed that the Ni and Mn were co-localized but that they were stored in distinctly different regions, indicating that the plant may detoxify these metals in metabolically different ways. Sunflower is one of the few plants known to accumulate Mn, storing and secreting the metal out of its glandular trichomes as MnO (54). Although the trichomes on the surface of *A. murale* are nonglandular and secretion is not possible, accumulation within the cells associated with these structures suggested that they may still have a functional role in metal storage and detoxification.

To determine if the patterns of Ni distribution observed in the fluorescent CMT images were consistent throughout the entire leaf, absorption-edge CMT was used. Movie 1 (see Supporting Information) and parts a–f of Figure 3 show that there are three distinct occurrences of Ni. First, as was seen in the fluorescence CMT images, enrichment of Ni occurs within the epidermal layers evidenced as a thin, brighter outline (more evident in Movie 1), surrounding the central tissues. Second, there are small, highly concentrated regions of Ni within the epidermal tissues of the entire leaf, appearing as bright white spots in the reconstructed leaf cross-section (black arrows Figure 3f). These Ni enrichments most likely correspond with Mn at the base of the calcium-rich trichomes (circles in Figure 2, Ca, Mn, Ni), as was observed in the fluorescent CMT images. Third, Ni enrichments occur in isolated regions within the interior of the leaf, possibly associated with the vascular system (white arrows in parts d and f of Figure 3 and Movie 1 of Supporting Information). However, the omnipresent pattern of Ni enrichment as-

sociated with the vascular tissues seen in the fluorescence tomograms (Figure 2) is less evident in the absorption-edge series (Figure 3 and Movie 1 of Supporting Information) resulting because the Ni concentration in the majority of this material is below the detection limit of absorption-edge CMT ($\sim 5000 \mu\text{g g}^{-1}$). Thus, only the most concentrated regions of Ni enrichment within the vascular system were resolved in the absorption-edge images.

The leaf used in the absorption-edge measurement contained on average 0.8% Ni, with a maximum of $\sim 8\%$, corresponding to 2.4 and 24% dry weight, respectively (see methods for wet weight conversion), and are some of the highest Ni concentrations reported in “fresh” plant tissues (37, 49). These values are higher than those for the leaf used in the fluorescence tomograms ($\sim 500 \mu\text{g g}^{-1}$), reflecting the difference in the soil Ni concentrations used in growing the plants.

In addition to vascular enrichment, accumulation of Ni within the tip of selected leaves was observed (Figure 3b). Nickel accumulation in the tip most likely results from a combination of both transport and storage mechanisms. The transport and delivery of Ni to the leaves probably occurs as mass flow through the xylem, driven by transpiration. Evidence for this is the presence of Ni within the xylem vesicles of the stem (Figure 4). Transpirational flow has been similarly implicated in the transport of Cd to the shoots of Indian mustard (*Brassica juncea*) (55) and for several other elements including B, Ca, Mn, and Si (56). As discussed previously, once Ni enters the leaves, it is sequestered into the epidermal vacuoles, away from the mesophyll (as seen in Figure 2). However, the vacuoles are a finite reservoir and, if transpirational delivery of Ni is unceasing, could reach capacity. The mechanisms for coping with excess (i.e., beyond which even a hyperaccumulator can tolerate) leaf Ni are unclear. One possibility is that excess Ni escapes the leaves via leaf venation terminals (hydathodes) in guttation fluids. Mizuno et al. (57) examined the guttation fluid of several plant species growing in ultramafic soils and found elevated levels of both Ni and Mn. They suggested that guttation acts as a method of expelling elements carried in the transpiration stream that are in excess of plant requirements. This would explain the abundance of Ni on/in *A. murale* leaf tips observed in this study. Since Ni delivery to the leaves is dependent upon transpiration, factors affecting transpiration (i.e., full

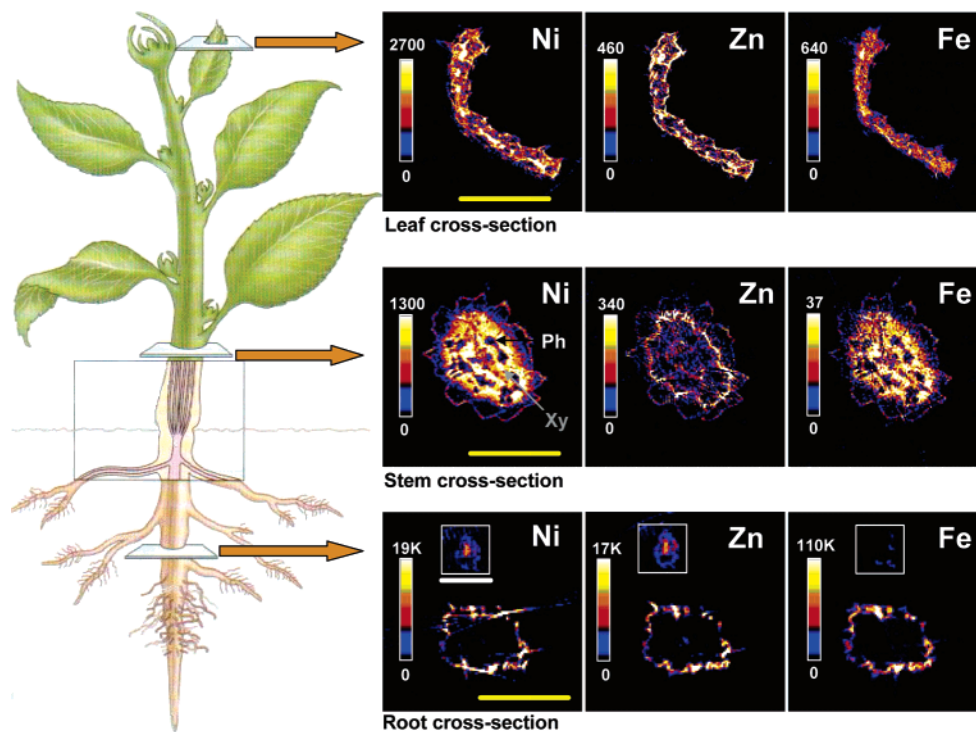


FIGURE 4. Ni, Fe, and Zn fluorescence CMT images of a leaf, stem, coarse and fine root cross-sections from *Alyssum murale* “Kotodesh”. Inset in root tomogram is of a finer root. The colorimetric scale maps region-specific relative metal concentrations ($\mu\text{g g}^{-1}$) for each element, with brighter colors indicating areas of higher enrichment. The slight streakiness of the coarser root Ni image is most likely due to beam hardening by very high Ni spots on the root surface. The lower thresholds for the tomograms were adjusted up slightly to suppress background noise and thereby improve image quality. The yellow scale bar represents $\sim 500\ \mu\text{m}$; the white scale bar (root inset) represents $\sim 100\ \mu\text{m}$. Plant figure adapted from *Plant Physiology*, 3rd ed., Tiaz and Zeiger (editors) with permission from Sinauer Associates, Inc., Publishers.

sun or shade) would have an impact on the total metal content and could explain why we found enrichment of Ni in some leaf tips and not others. However, Kovacheva et al. (58) pointed out that there are several factors such as biological variety, seasonal and climatic changes, age and height of sampling, and soil conditions that can influence the distribution of metals and nutrients within plant organs. Boyd et al. (59) and more recently Kupper et al. (60) also found age-dependent changes in metal concentrations, generally with older leaves exhibiting higher and more segregated metal concentrations than younger.

Further analysis is necessary to evaluate the role of transpiration and guttation in controlling the compartmentalization of Ni within the leaves of *A. murale*. In addition, the contribution of the regions of highest Ni enrichment (leaf tip, trichome) to the overall distribution of Ni within the leaf should be assessed to explore their significance as a mechanism for Ni tolerance.

Metal Compartmentalization in Stems and Roots. We also used fluorescence microtomography to explore the distribution of metals in the stem and root tissues of *A. murale* “Kotodesh” as shown in Figure 4. The epidermis of the stem has pulled away from the cortex, most likely as a result of the drying process, and can be seen as a thin jagged line enriched in Ni. Nickel is also concentrated in the xylem (black arrow Figure 4) and absent from the phloem (gray arrow, Figure 4) and cortex. In the roots of *A. murale*, Ni is isolated in the stele or vascular tissues of the finer root (Figure 4 inset in root tomogram), with very little metals on the exterior. The opposite pattern is seen for the coarser root, which is devoid of metals on the interior but covered in a “coating” of well-correlated Fe, Zn, and Ni. The presence of these metals on/in the exterior of the root could have resulted from numerous processes including sorption, precipitation, microbial activity, or inadequate washing. Further analysis is under way to verify

the relationship (if any) between root coatings and the uptake of Ni from the surrounding environment, especially since no coating was found on the finer roots possessing vascular enrichment.

This research clearly highlights the applicability of synchrotron-based tomographic techniques to the study of metal partitioning within hyperaccumulating plant tissues. Synchrotron fluorescence microtomography provided highly sensitive, quantitative, multi-element, tissue-specific images of the metal distributions in leaf, stem, and root tissues. Absorption-edge CMT allowed us, for the first time, to resolve the in vivo metal distributions three-dimensionally, highlighting the variability of the highest metal concentrations. The results are consistent with a transport model involving uptake of Ni by roots, transport through the stem xylem to the shoots, where it is then distributed through the veins to the dermal tissues, and in some cases leaf tips. Verification of these findings with additional analysis is required, particularly to explore further how factors affecting transpiration and guttation may control the distribution of Ni (and possibly other metals) in/on the tips of *A. murale* leaves. Furthermore, examination of more extensive sections of roots from both soil and hydroponic mediums should be done to help identify the section/s of the root that are the most transport active with respect to Ni as well as the ubiquity or uniformity of the mixed metal “coatings” observed in/on the coarser roots. It is clear, even from this small data set, that the variability of metal distributions within plant tissues can differ, not only between the roots, stems, and shoots but also within individual organs. Understanding this variability is important in elucidating how hyperaccumulating plants cope with foliar metal concentrations grossly beyond the physiological needs of most plants. Together, fluorescence and absorption-edge CMT provide a valuable method for exploring this variability and are uniquely suited for eluci-

dating and quantifying the microdistributions of multiple metals and determining the ubiquity of these distributions, within specific tissues of intact hyperaccumulating plant tissues.

Acknowledgments

We are thankful to Dr. Kirk Cyzmeck (Delaware Biotechnology Institute) for help with acquiring SEM images of leaf cross sections and to the reviewers for constructive feedback during the writing process. The microtomography image was performed at GeoSoilEnviroCARS (Sector 13), Advanced Photon Source (APS), Argonne National Laboratory. GeoSoilEnviroCARS is supported by the National Science Foundation - Earth Sciences (EAR-0217473), Department of Energy - Geosciences (DE-FG02-94ER14466) and the State of Illinois. Use of the APS was supported by the U.S. Department of Energy, Basic Energy Sciences, Office of Energy Research, under Contract No. W-31-109-Eng-38.

Supporting Information Available

An absorption-edge CMT movie showing the Ni distribution/concentration as a sequence of projections from the tip to the proximal end in a "fresh" *Alyssum murale* "Kotodesh" leaf with brighter regions indicating higher ($>5000 \mu\text{g g}^{-1}$) Ni enrichment, the maximum of which was 7.9% wet weight (~40% dry weight). This material is available free of charge via the Internet at <http://pubs.acs.org>.

Literature Cited

- Chaney, R. L.; Malik, M.; Li, Y. M.; Brown, S. L.; Brewer, E. P.; Angle, J. S.; Baker, A. J. Phytoremediation of soil metals. *Curr. Opin. Biotechnol.* **1997**, *8*, 279–284.
- Li, Y. M.; Chaney, R. L.; Brewer, E.; Roseberg, R.; Angle, J. S.; Baker, A. J. M.; Reeves, R.; Nelkin, J. Development of a technology for commercial phytoextraction of nickel: economic and technical considerations. *Plant Soil.* **2003**, *249*, 107–115.
- Banuelos, G. S.; Ajwa, H. A.; Terry, N.; Zayed, A. Phytoremediation of selenium laden soils: A new technology. *J. Soil Water Conserv.* **1997**, *52*, 426–430.
- Tu, C.; Ma, L. Q.; Bondada, B. Arsenic accumulation in the hyperaccumulator Chinese brake and its utilization potential for phytoremediation. *J. Environ. Qual.* **2002**, *31*, 1671–1675.
- Brooks, R. R.; Lee, J.; Reeves, R. D.; Jaffre, T. Detection of nickeliferous rocks by analysis of herbarium specimens of indicator plants. *J. Geochem. Explor.* **1977**, *7*, 49–57.
- Kerkeb, L.; Kramer, U. The role of free histidine in xylem loading of nickel in *Alyssum lesbiacum* and *Brassica juncea*. *Plant Physiol.* **2003**, *131*, 716–724.
- Kramer, U.; Cotter-Howells, J. D.; Charnock, J. M.; Baker, A. J. M.; Smith, J. A. C. Free histidine as a metal chelator in plants that accumulate nickel. *Nature* **1996**, *379*, 635–638.
- Lombi, E.; Zhao, F. J.; McGrath, S. P.; Young, S. D.; Sacchi, G. A. Physiological evidence for a high-affinity cadmium transporter highly expressed in a *Thlaspi caerulescens* ecotype. *New Phytol.* **2001**, *149*, 53–60.
- Salt, D. E.; Prince, R. C.; Baker, A. J. M.; Raskin, I.; Pickering, I. J. Zinc ligands in the metal hyperaccumulator *Thlaspi caerulescens* as determined using X-ray absorption spectroscopy. *Environ. Sci. Technol.* **1999**, *33*, 713–717.
- Kupper, H.; Lombi, E.; Zhao, F. J.; McGrath, S. P. Cellular compartmentation of cadmium and zinc in relation to other elements in the hyperaccumulator *Arabidopsis halleri*. *Planta* **2000**, *212*, 75–84.
- Kramer, U.; Grime, G. W.; Smith, J. A. C.; Hawes, C. R.; Baker, A. J. M. Micro-PIXE as a technique for studying nickel localization in leaves of the hyperaccumulator plant *Alyssum lesbiacum*. *Nucl. Instrum. Methods Phys. Res., Sect. B* **1997**, *130*, 346–350.
- Liu, D. H.; Kottke, I. Subcellular localization of Cd in the root cells of *Allium sativum* by electron energy loss spectroscopy. *J. Biosci.* **2003**, *28*, 471–478.
- Pickering, I. J.; Prince, R. C.; Salt, D. E.; George, G. N. Quantitative, chemically specific imaging of selenium transformation in plants. *Proc. Natl. Acad. Sci. U.S.A.* **2000**, *97*, 10717–10722.
- Scheckel, K. G.; Lombi, E.; Rock, S. A.; McLaughlin, N. J. In vivo synchrotron study of thallium speciation and compartmentation in *Iberis intermedia*. *Environ. Sci. Technol.* **2004**, *38*, 5095–5100.
- Howe, J. A.; Loeppert, R. H.; Derose, V. J.; Hunter, D. B.; Bertsch, P. M. Localization and speciation of chromium in subterranean clover using XRF, XANES, and EPR spectroscopy. *Environ. Sci. Technol.* **2003**, *37*, 4091–4097.
- McLain, A. A.; Altman, S. A.; Rivers, M. L.; Cygab, R. T. Use of computerized microtomography to examine the relationships of sorption sites in alluvial soils to iron and pore space distributions; *NUREG/CR-6784*; US Nuclear Regulatory Commission: Washington, DC, 2002.
- Flynn, G. F.; Rivers, M. L.; Sutton, S. R.; Eng, P.; Klock, W. X-ray computed microtomography (CMT): a noninvasive screening tool for characterization of returned rock cores from mars and other solar system bodies. *Lunar and Planetary Science XXXI. LP1 #1893*; Houston, TX 2000.
- Hansel, C. M.; Fendorf, S. Characterization of Fe plaque and associated metals on the roots of mine-waste impacted aquatic plants. *Environ. Sci. Technol.* **2001**, *35*, 3863–3868.
- Hansel, C. M.; LaForce, M. J.; Fendorf, S.; Sutton, S. Spatial and temporal association of As and Fe species on aquatic plant roots. *Environ. Sci. Technol.* **2002**, *36*, 1988–1994.
- Keon-Blute, N.; Brabander, D. J.; Hemond, H. F.; Sutton, S. R.; Newville, M.; Rivers, M. Arsenic sequestration by ferric iron plaque on cattail roots. *Environ. Sci. Technol.* **2004**, *38*, 6074–6077.
- Kukier, U.; Chaney, R. L. Amelioration of nickel phytotoxicity in muck and mineral soils. *J. Environ. Qual.* **2001**, *30*, 1949–1960.
- Chaney, R.; Angle, J.; Baker, A.; Li, Y. Method for phytomining of nickel, cobalt, and other metals from soil. U.S. Patent 5,944,872, August 31, 1999.
- Li, Y. M.; Chaney, R. L.; Brewer, E. P.; Angle, J. S.; Nelkin, J. Phytoextraction of nickel and cobalt by hyperaccumulator *Alyssum* species grown on nickel-contaminated soils. *Environ. Sci. Technol.* **2003**, *37*, 1463–1468.
- Flannery, B. P.; Deckman, H. W.; Roberge, W. G.; D'Amico, K. L. Three-dimensional X-ray microtomography. *Science* **1987**, *237*, 1439–1444.
- Kinney, J. H.; Haupt, D. L.; Nichols, M. C.; Breunig, T. M.; Marshall, G. W. M.; Marshall, S. J. The X-ray tomographic microscope: three-dimensional perspectives of evolving microstructures. *Nucl. Instrum. Methods Phys. Res., Sect. A* **1994**, *347*, 480–486.
- Rivers, M. L.; Sutton, S. R.; Eng, P. Geoscience applications of X-ray computed microtomography. Proceedings of SPIE, Developments in X-ray tomography II, **1999**, 3772, 78–86.
- Sutton, S. R.; Bertsch, P. M.; Newville, M.; Rivers, M.; Lanzirrotti, A.; Eng, P. Microfluorescence and microtomography analyses of heterogeneous earth and environmental materials. Proceedings of SPIE, Applications of Synchrotron Radiation in Low-Temperature & Environmental Science, **2002**, 49, 429–483.
- Eng, P. J.; Newville, M.; Rivers, M. L.; Sutton, S. R. Dynamically figured Kirkpatrick Baez micro-focusing optics. X-ray Micro-focusing: Applications and Technique. *SPIE Proc.* **1998**, 3449, 145.
- Eng, P. J.; Rivers, M.; Yang, B. X.; Schildkamp, W. Micro-focusing 4keV to 65keV X-rays with bent Kirkpatrick-Baez mirrors. X-ray microbeam technology and applications. *SPIE Proc.* **1995**, 2516, 41–51.
- Kirkpatrick, P.; Baez, A. V. Formation of optical images by X-rays. *J. Opt. Soc. Am.* **1948**, *38*, 766.
- Dowd, B. A.; Campbell, G. H.; Marr, R. B.; Nagarkar, V. V.; Tipnis, S. V.; Axe, L.; Siddons, D. P. Developments in synchrotron X-ray computed microtomography at the National Synchrotron Light Source. Proceedings of SPIE, Developments in X-ray Tomography II, **1999**, 3772, 224–236.
- Golosio, B.; Simionovici, A.; Somogyi, A.; Lemelle, L.; Chukalina, M.; Brunetti, A. Internal elemental microanalysis combining X-ray fluorescence, Compton and transmission tomography. *J. Appl. Phys.* **2003**, *94*, 145–157.
- Hogan, J. P.; Gonsalves, R. A.; Krieger, A. S. Fluorescent computer tomography: a model for correction of X-ray absorption. *IEEE Trans. Nucl. Sci.* **1991**, *36*, 1721–1727.
- La Riviere, P. J.; Billmire, D. M. Penalized-likelihood image reconstruction for X-ray fluorescence computed tomography with unknown fluorescence attenuation maps. Proceedings of SPIE, Developments in X-ray Tomography IV, **2004**, 5535, 243–252.
- Rivers, M.; Wang, Y.; Uchida, T. Microtomography at GeoSoil-EnviroCARS. Proceedings of SPIE, Developments in X-ray tomography IV, **2004**, 5535, 783–791.

- (36) Cloetens, P.; Boller, E.; Ludwig, W.; Baruchel, J.; Schlenker, M. Absorption and phase imaging with synchrotron radiation. *Europhys. News* **2001**, *32*.
- (37) Broadhurst, C.; Chaney, R.; Angle, J. S.; Maugel, T.; Erbe, E.; Murphy, C. Simultaneous hyperaccumulation of Nickel, Manganese, and Calcium in *Alyssum* leaf trichomes. *Environ. Sci. Technol.* **2004**, *38*, 5797.
- (38) Kupper, H.; Zhao, F. J.; McGrath, S. P. Cellular compartmentation of zinc in leaves of the hyperaccumulator *Thlaspi caerulescens*. *Plant Physiol.* **1999**, *119*, 305–311.
- (39) Kupper, H.; Lombi, E.; Zhao, F. J.; Wieshammer, G.; McGrath, S. P. Cellular compartmentation of nickel in the hyperaccumulators *Alyssum lesbiacum*, *Alyssum bertolonii* and *Thlaspi goesingense*. *J. Exp. Bot.* **2001**, *52*, 2291–2300.
- (40) Heath, S. M.; Southworth, D.; Dallura, J. A. Localization of nickel in epidermal subsidiary cells of leaves of *Thlaspi montanum* var *siskiyouense* (Brassicaceae) using energy-dispersive X-ray microanalysis. *Int. J. Plant Sci.* **1997**, *158*, 184–188.
- (41) Taiz, L.; Zeiger, E. *Plant Physiology*, 3rd ed.; Sinauer Associates, Inc.: Sunderland, Massachusetts, 2002.
- (42) Prasad, M. N. V.; Strzalka, K. *Heavy Metal Stress in Plants: From Molecules to Ecosystems*; 2nd ed.; Springer: Berlin, 2004.
- (43) Jhee, E. M.; Dandridge, K. L.; Christy, A. M., Jr.; Pollard, J. A. Selective herbivory on low-zinc phenotypes of the hyperaccumulator *Thlaspi caerulescens* (Brassicaceae). *Chemoecology* **1999**, *9*, 93–95.
- (44) Pollard, A. J.; Baker, A. J. M. Deterrence of herbivory by zinc hyperaccumulation in *Thlaspi caerulescens* (Brassicaceae). *New Phytol.* **1997**, *135*, 655–658.
- (45) Boyd, R. S.; Moar, W. J. The defensive function of Ni in plants: response of the polyphagous herbivore *Spodoptera exigua* (Lepidoptera: Noctuidae) to hyperaccumulator and accumulator species of *Streptanthus* (Brassicaceae). *Oecologia.* **1999**, *118*, 218–224.
- (46) Boyd, R. S.; Davis, M. A.; Wall, M. A.; Balkwill, K. Nickel defends the South African hyperaccumulator *Senecio coronatus* (Asteraceae) against *Helix aspersa* (Mollusca: Pulmonidae). *Chemoecology.* **2002**, *12*, 91–97.
- (47) Davis, M. A.; Boyd, R. S. Dynamics of Ni-based defense and organic defenses in the Ni hyperaccumulator, *Streptanthus polygaloides* (Brassicaceae). *New Phytol.* **2000**, *146*, 211–217.
- (48) Lee, J.; Reeves, R. D.; Brooks, R. R.; Jaffre, T. Relation between Nickel and Citric-Acid in Some Nickel-Accumulating Plants. *Phytochemistry* **1978**, *17*, 1033–1035.
- (49) Sagner, S.; Kneer, R.; Wanner, G.; Cosson, J. P.; Deus-Neumann, B.; Zenk, M. H. Hyperaccumulation, complexation and distribution of nickel in *Sebertia acuminata*. *Phytochemistry* **1998**, *47*, 339–347.
- (50) Kersten, W. J.; Brooks, R. R.; Reeves, R. D.; Jaffre, T. Nature of nickel-complexes in *Psychotria douarrei* and other nickel-accumulating plants. *Phytochemistry* **1980**, *19*, 1963–1965.
- (51) Levin, D. A. The role of trichomes in plant defense. *Quart. Rev. Biol.* **1973**, *48*, 3–15.
- (52) Lanning, F. C. Calcite in *Lesquerella ovalifolia* trichomes. *Science* **1961**, *133*, 380.
- (53) Psaras, G. K.; Constantinidis, T.; Cotsopoulos, B.; Manetas, Y. Relative abundance of nickel in the leaf epidermis of eight hyperaccumulators: evidence that the metal is excluded from both guard cells and trichomes. *Ann. Bot. London.* **2000**, *86*, 73–78.
- (54) Blamey, F. P. C.; Joyce, D. C.; Edwards, D. B.; Asher, C. J. Role of trichomes in sunflower tolerance to manganese toxicity. *Plant Soil* **1986**, *91*, 171–180.
- (55) Salt, D. E.; Prince, R. C.; Pickering, I. J.; Raskin, I. Mechanisms of cadmium mobility and accumulation in Indian Mustard. *Plant Physiol.* **1995**, *109*, 1427–1433.
- (56) Marschner, H. *Mineral Nutrition of Higher Plants*, 2nd ed.; Academic Press: San Diego, CA, 1995.
- (57) Mizuno, N.; Takahashi, A.; Wagatsuma, T.; Mizuno, T.; Obata, H. Chemical composition of guttation fluid and leaves of *Petasites japonicus* v. *giganteus* and *Polygonum cuspidatum* growing on ultramafic soil. *Soil Sci. Plant Nutr.* **2002**, *48*, 451–453.
- (58) Kovacheva, P.; Rumiana, D.; Ivelin, K. On the representative sampling of plants for multielement analysis. *Phytol. Balcan.* **2000**, *6*, 91–102.
- (59) Boyd, R. S.; Jaffre, T.; Odom, J. W. Variation in nickel content in the nickel-hyperaccumulating shrub *Psychotria douarrei* (Rubiaceae) from New Caledonia. *Biotropica* **1999**, *31*, 403–410.
- (60) Kupper, H.; Mijovilovich, A.; Meyer-Klaucke, W.; Kroneck, P. M. H. Tissue- and age-dependent differences in the complexation of cadmium and zinc in the cadmium/zinc hyperaccumulator *Thlaspi caerulescens* (Ganges ecotype) revealed by X-ray absorption spectroscopy. *Plant Physiol.* **2004**, *134*, 748–757.

Received for review May 28, 2004. Revised manuscript received December 21, 2004. Accepted January 4, 2005.

ES0492034